Electronic Supplementary Material (ESI) for Journal of Materials Chemistry A.

Non-oxidative calcination enhances methane dry reforming performance of Ni/CeO_{2-x} catalysts under thermal and photo-thermal conditions

Kristijan Lorber[1,2], Vasyl Shvalya[3], Janez Zavašnik[3], Damjan Vengust[3], Iztok Arčon[2,3], Matej Huš[1,4,5], Andraž Pavlišič[1], Janvit Teržan[1], Uros Cvelbar[3], Blaž Likozar[1] and Petar Djinović[1,2]*

[1]National Institute of Chemistry, Hajdrihova 19, 1000 Ljubljana, Slovenia

[2]University of Nova Gorica, Vipavska 13, SI-5000 Nova Gorica, Slovenia

[3]Jožef Stefan Institute, Jamova cesta 39, SI-1000 Ljubljana, Slovenia

[4]Association for Technical Culture (ZOTKS), Založka 65, 1000 Ljubljana, Slovenia

[5]Institute for the Protection of Cultural Heritage (ZVKDS), Poljanska 40, 1000 Ljubljana, Slovenia

Corresponding author e-mail: petar.djinovic@ki.si

Conversion, rate and H_2/CO calculations

The conversion of CH_4 and CO_2 were calculated by Eq. 1,

$$X_{CH_4,CO_2} = \frac{1 - C_A/C_{A0}}{1 + \varepsilon_A C_A/C_{A0}} * 100\% \quad (1)$$

C_{A0} is the starting concentration of CH_4 or CO_2,

C_A is the measured concentration of CH_4 or CO_2 during reaction and

ε_A is the expansion factor, which in chase of DRM equals 1.

$CH_4 + CO_2 \leftrightarrow 2H_2 + 2CO$

ε_A=[∑moles of products - ∑moles of reactants]/ ∑moles of reactants = (4-2)/2= 1

For background on the derivation of the calculation see reference[1].

Reaction rates for CH_4, CO_2, CO and H_2 were calculated by considering conversion (X_A), mass of catalyst ($m_{cat.}$), flow rate (F_A) as well as constant of molar volume of gas (0,0446 mol/L) according to Eq.2:

$$r_A = \frac{X_A * F_A * 0.0446}{m_{cat.}}, \left[\frac{mmol}{g * min}\right] \quad (2)$$

The H_2 selectivity is expressed as H_2/CO ratio and was calculated as a ratio between rates of H_2 and the rates of CO as shown in Eq. 3,

$$\frac{H_2}{CO} = \frac{rH_2}{rCO} \quad (3)$$

Energy efficiency calculation

$$CH_4 + CO_2 \leftrightarrow 2H_2 + 2CO \quad (4)$$

-x -x 2x 2x

$$CO_2 + H_2 \leftrightarrow CO + H_2O \quad (5)$$

-y -y y y

By combining (H_2) = 2x − y, (CO) = 2x + y and (H_2O) = y, we calculated the individual rates:

$$r(CH_4) = \frac{r(H_2) + r(CO)}{4} \quad (6)$$

$$r(CO_2) = \frac{3r(CO) - r(H_2)}{4} \quad (7)$$

$$r(H_2O) = \frac{r(CO) - r(H_2)}{2} \quad (8)$$

The H_2/CO ratio reflects the selectivity of catalysts and is expressed as:

$$H_2/CO = r(H_2)/r(CO) \quad (9)$$

The light to fuel efficiency (η) of light-assisted DRM reaction

$$\eta = \frac{rH2 * \Delta_c H^0_{H2} + rCO * \Delta_c H^0_{CO} - rCH4 * \Delta_c H^0_{CH4}}{light\ power} * 100\ \% \quad (10)$$

Where standard heat of combustion ($\Delta_c H^0$, 298.15 K) or higher heating values for the CO, H_2, and CH_4 fuels are:

$\Delta_c H^0_{H2}$ = 283.0 kJ mol^{-1}

$\Delta_c H^0_{CO}$ = 285.8 kJ mol^{-1}

$\Delta_c H^0_{CH4}$ = 890.8 kJ mol^{-1}

CO_2 is not considered as a fuel ($\Delta_c H^0$ = 0)

Light power is the power emitted by the LED source: 108 mW/cm^2 for λ=400-450 nm; 535 mW/cm^2 for λ=450-700 nm and 780 mW/cm^2 for λ=400-700 nm.

The production rates for r(H_2) and r(CO) are 4.33 mmol/g_{cat}*min and 5.87 mmol/g_{cat}*min, reaction rates for r(CH_4) and r(CO_2) are 2.33 mmol/g_{cat}*min and 3.47 mmol/g_{cat}*min at 460°C, λ=400-450 nm and 108 mW/cm^2 light power. The rates are the difference between photo-thermal and thermocatalytic rates at identical catalyst temperatures. The light-to-fuel efficiency (η) was calculated to be 24.5 % for NC-H_2 catalyst at 460°C during λ=400-450 nm illumination. In a similar manner, light-to-fuel efficiency calculations for other tested catalysts using different temperatures and illuminations were performed.

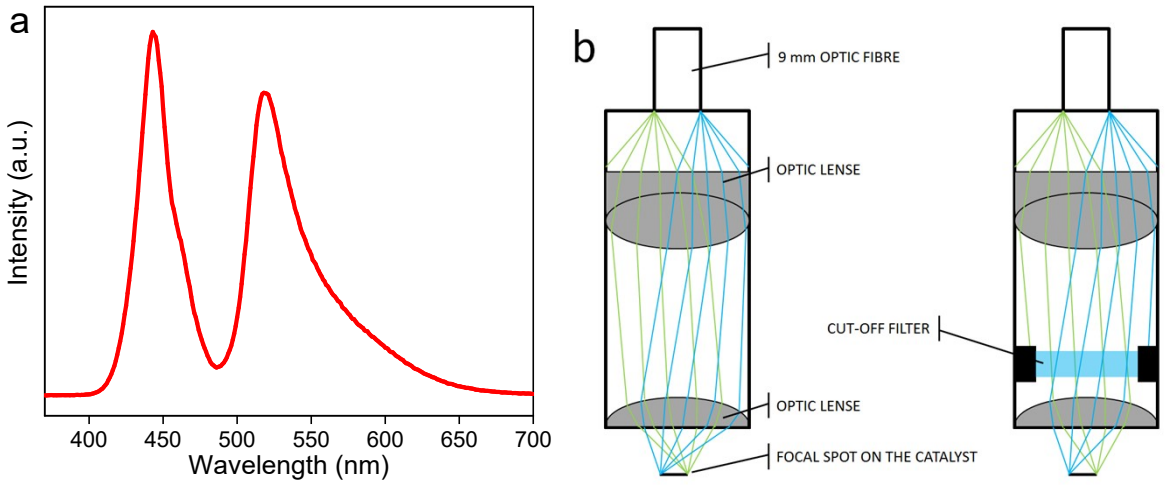

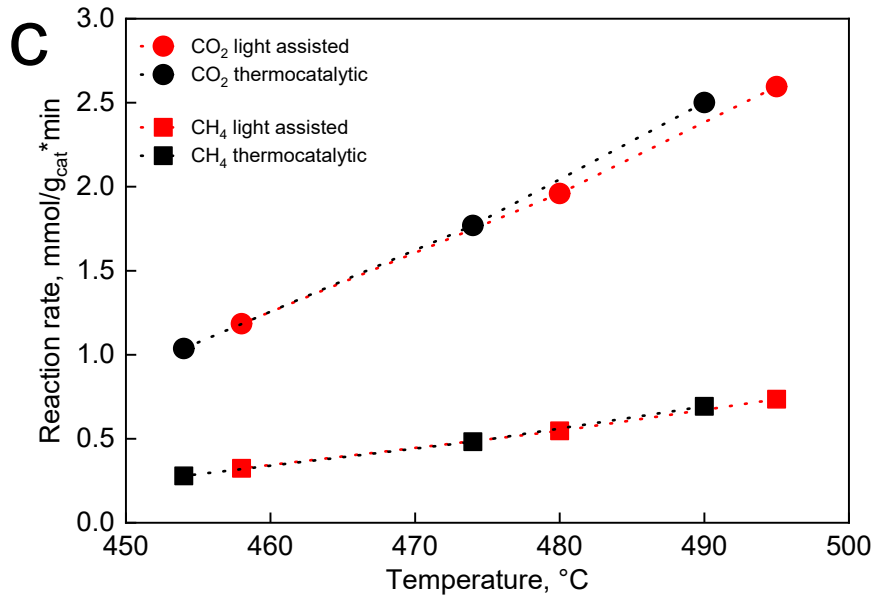

Figure S1. a) Emission spectrum from the Schott KL2500 LED light that was used for photo-thermal catalytic experiments.

b) Schematic of the optics used to focus the light over the catalyst sample.

c) Methane and CO_2 rates during thermo-catalytic (black symbols) and light assisted DRM reaction (red symbols) over $2Ni/SiO_2$ catalyst. Reaction conditions: 2 mg of catalyst, $\Phi(CH_4)=\Phi(CO_2)=$ 10ml/min. Prior to catalytic tests, the sample was activated *in-situ* for 30 min at 450 °C in a 10 ml/min flow of 5% H_2/N_2. During the light-assisted experiment, the catalyst was illuminated by 780 mW/cm^2 of white light.

By inserting the cut-off filter for the wavelength dependent experiments, part of the light is blocked (Figure S1b), which results in loss of optic power. As a result, the sum of 400-450 nm and 450-700 nm irradiances (108 mW/cm^2 and 535 mW/cm^2) does not yield full spectrum irradiance (780 mW/cm^2).

The control experiment in Figure S1c shows the light-assisted DRM activity being benchmarked to the thermally driven reaction over the $2Ni/SiO_2$ catalyst. Silica is a wide bandgap insulator, and when coupled with poor visible light absorption of nickel, negligible photocatalytic activity gain is expected during this experiment. Indeed, the CH_4 and CO_2 rates differ by less than 5 % in thermal and light-assisted DRM experiments at identical catalyst temperatures, revealing the temperature measurement inside the catalyst layer reflects the local temperature at the metallic particles.

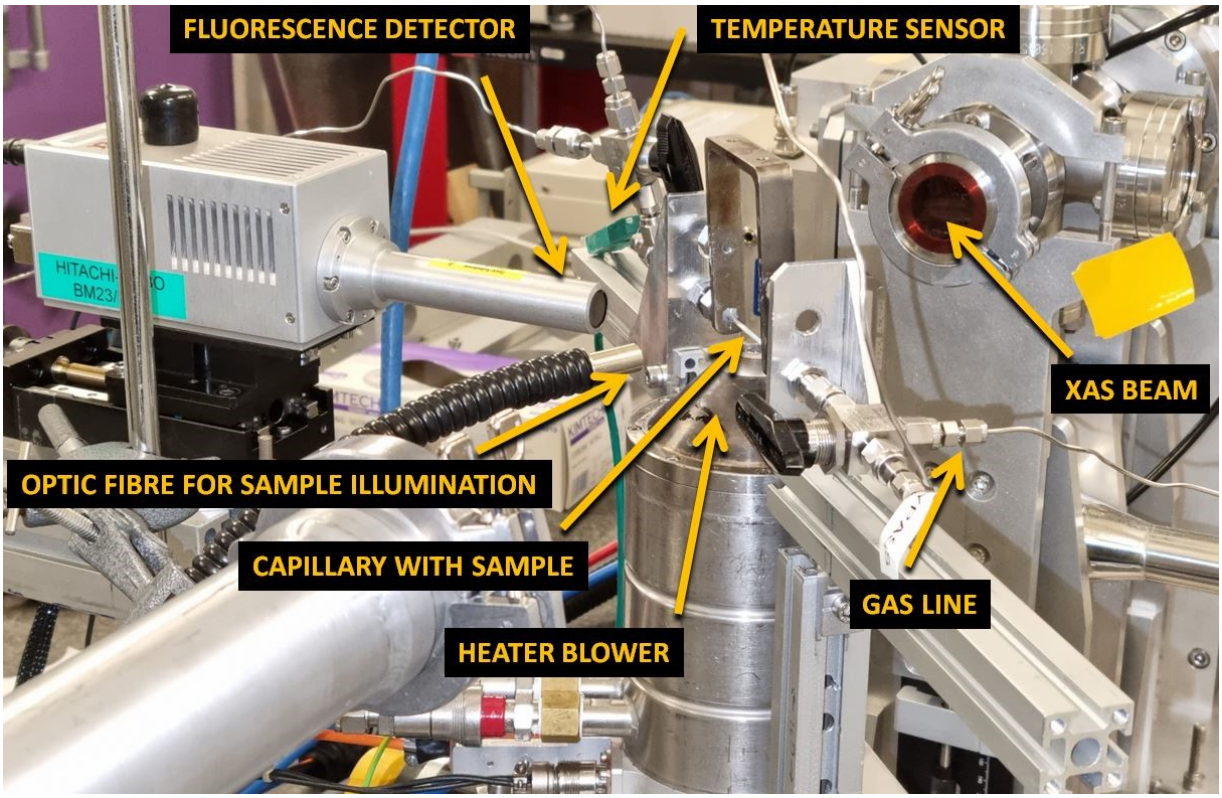

Figure S2. Setup for the *in-situ* XAS analysis of $2Ni/CeO_{2-x}$ catalysts at ESRF synchrotrone, BM23 beamline.

Supplementary note on the effect of calcination atmosphere on DRM catalytic activity

The methane conversion values during the thermocatalytic DRM reaction are compared for specific calcination sequences below. Note that catalyst activation directly prior to catalytic reaction, and reaction conditions were identical in all experiments.

CeO_2 calcination in H_2 → Ni/CeO_2 calcination in H_2 → activation → reaction
CeO_2 calcination in H_2 → Ni/CeO_2 calcination in air → activation → reaction
CeO_2 calcination in air → Ni/CeO_2 calcination in air → activation → reaction
CeO_2 calcination in H_2→ Ni/CeO_2 calcination in Ar→ activation → reaction
CeO_2 calcination in Ar→ Ni/CeO_2 calcination in Ar→ activation → reaction

We can see in Figure S3 that the second calcination process (calcination of Ni/CeO_2 material) determines the catalytic activity and is crucial. The initial calcination of bare ceria is of lesser relevance.

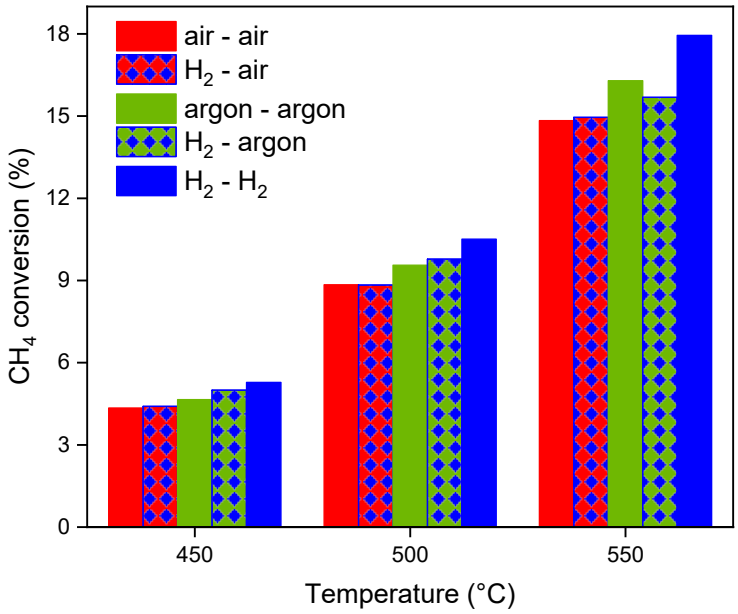

Figure S3. Methane conversion at different reaction temperatures for 2Ni/CeO_2-R catalysts calcined according to the following sequences: air → air (red), H_2 → air (red and blue), argon → argon (green), H_2 → argon (green and blue) and H_2 → H_2 (blue).

Equilibrium conversions and H_2/CO ratio were calculated based on the data provided by the Gaseq software. Equilibrium compositions are based on Gibbs free energy minimization under specified reaction conditions (temperature, pressure and initial gas composition). Figure S1 shows a temperature-dependent equilibrium composition during DRM reaction (equimolar CH_4 and CO_2 feed, 1 bar pressure), H_2, CO and water are reaction products. H_2/CO ratio (black squares) is calculated as a ratio between moles of H_2/moles of CO.

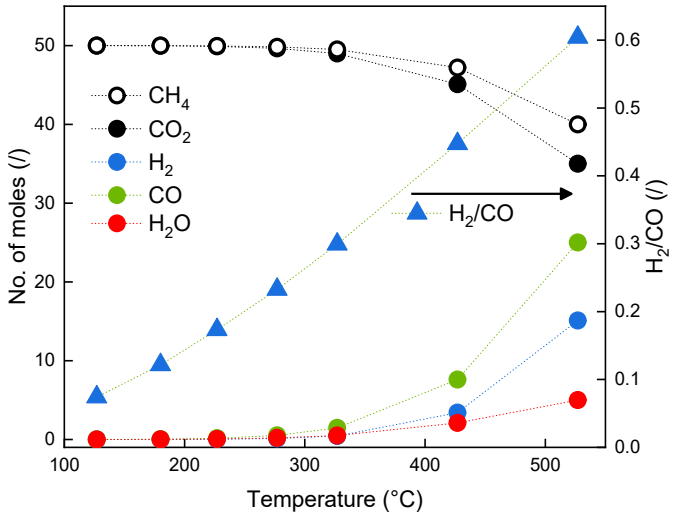

Figure S4. Number of moles as a function of temperature under thermodynamic equilibrium conditions during DRM reaction allowing for CO, H_2 and H_2O as reaction products. Lines guide the eye.

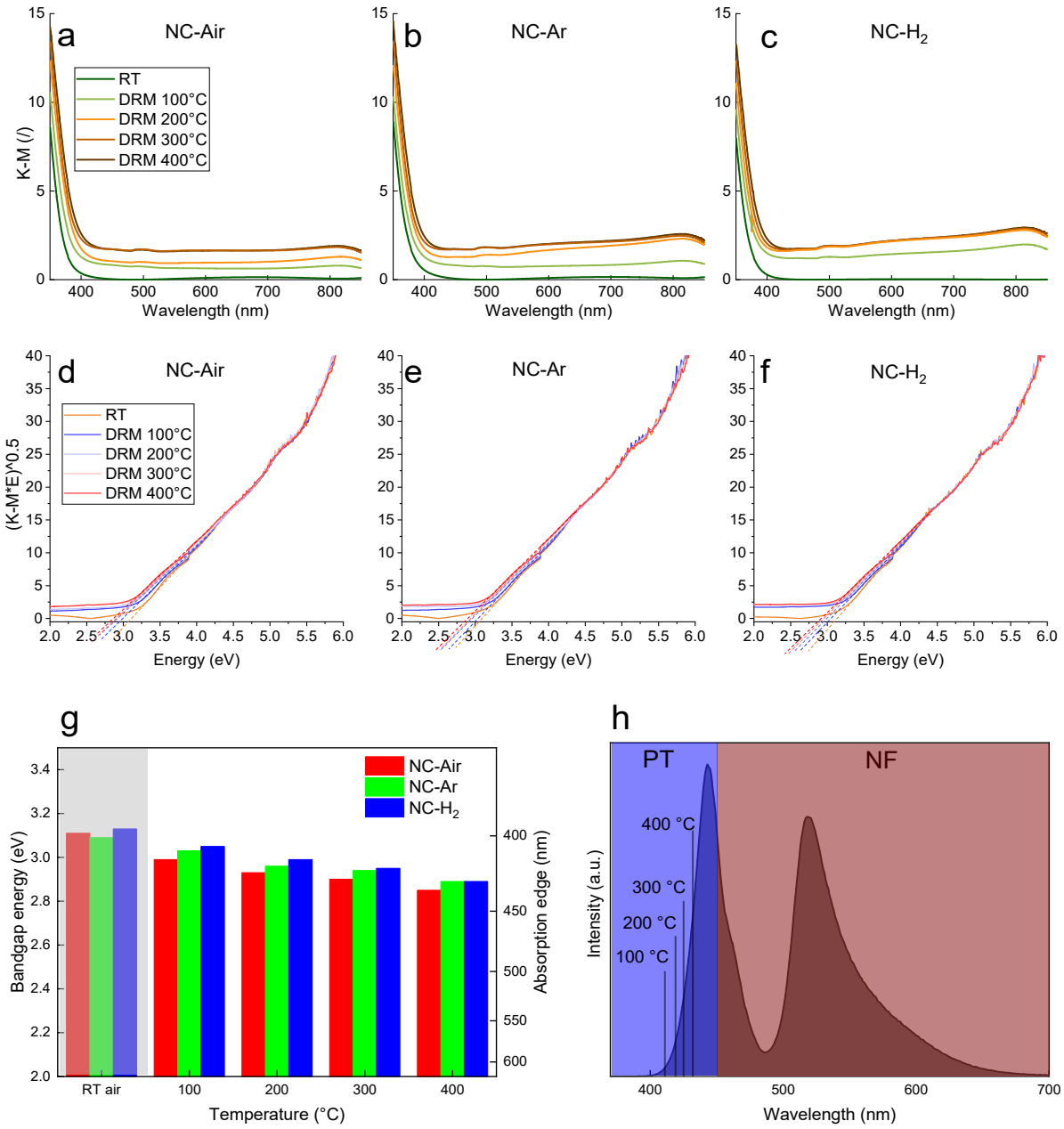

Figure S5. UV-Vis spectra of (a) NC-Air, (b) NC-Ar and (c) NC-H_2 recorded in air at room temperature and *in-situ* at different temperatures in CH_4/CO_2 flow. Tauc plot analysis of optical bandgap energies for (d) NC-Air, (e) NC-Ar and (f) NC-H_2 catalysts. (g) Bandgap values for the analyzed catalysts at different temperatures and atmospheres. (h) Emission spectrum of the light source. Blue and red rectangles show the range of wavelengths used to probe the PT and NF mechanisms. Vertical lines show the temperature dependent absorption edge of the 2Ni/CeO_{2-x} catalysts.

Supplementary note on Photoluminescence analysis

According to wavelength dependent light-to-fuel calculations, PT is the main driving force for increasing DRM rate during photo-thermal reaction. As it requires electron excitation across the bandgap to drive the reaction, we analyzed and compared the photoluminescence spectra of all three 2Ni/CeO_2 catalysts. Higher photoluminescence suggests more extensive emissive recombination of hot carriers in the sample.

The catalyst calcined in air exhibits the highest intensity of photoluminescence, followed by closely resembling samples calcined in argon and hydrogen (Figure S4). Highest photoluminescence suggests the highest extent of emissive recombination of hot carriers, meaning they are recombined before they can participate in the photocatalytic reaction. The increasing light-to-fuel efficiency and the decreasing PL intensity follow the same trend, suggesting more efficient charge segregation is the origin of more efficient photocatalytic reaction. The slower recombination is likely a consequence of smaller nickel clusters on ceria. With decreasing the metal particle size, the Fermi level of the semiconductor and metal equilibrate and smaller metal particles cause a larger shift of Fermi level to more negative potentials.[2] As a result of interfacial band bending between the n-type semiconductor (ceria) and metallic nickel, a Schottky barrier is formed, and that is higher with a more pronounced up-shift. Higher Schottky barrier more efficiently prevents carrier recombination, leading to more efficient photocatalysis.[3]

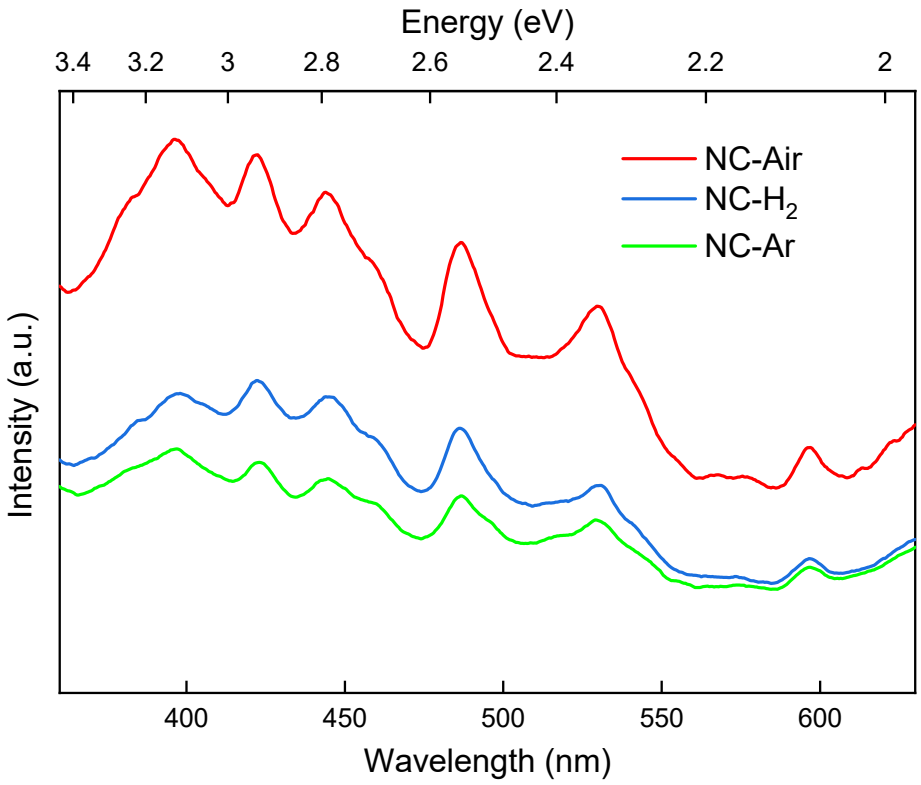

Figure S6. Photoluminescence spectra of the 2Ni/CeO_2 catalysts calcined in different atmospheres.

Pulse CO_2 activation

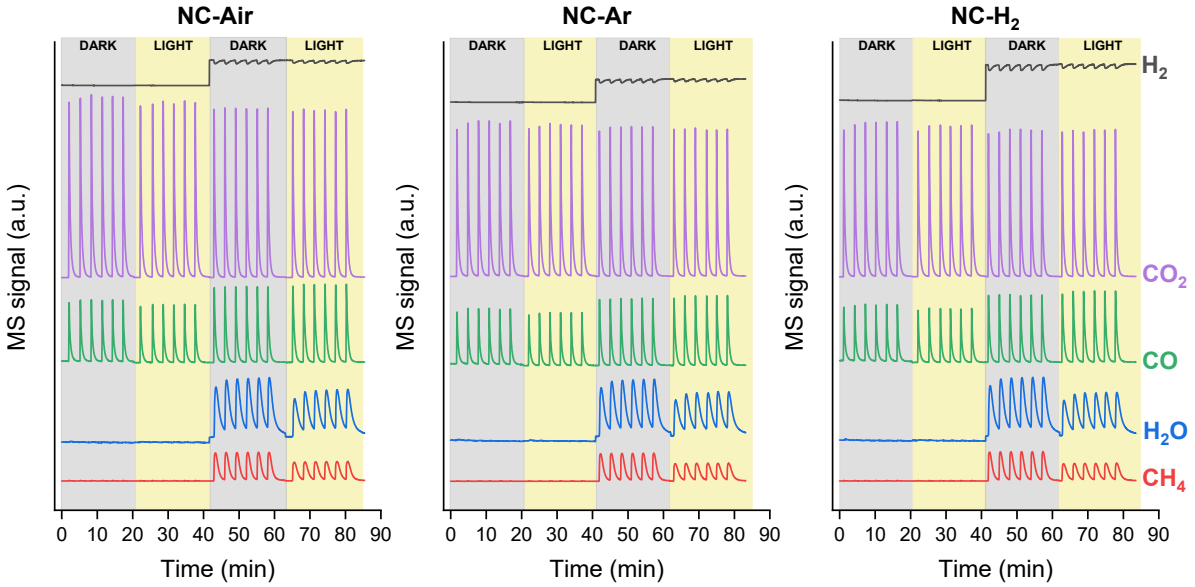

Figure S7. CO_2 pulse reaction mimicking RWGS reaction under thermal and photo-thermal conditions (2mg of catalyst, irradiated with 613 mW of white light, 400 > λ >700 nm) at a constant catalyst temperature of 400 °C during Ar flow (first 40 minutes of experiment) and 5% H_2/Ar flow over NC-Air, NC-Ar and NC-H_2 catalysts. Individual signals are scaled for better visualization.

CO_2 pulsing over the catalysts in argon flow at 400°C in dark or when illuminated produces no CO or methane, revealing light and catalyst alone cannot dissociate carbon dioxide. The CO m/z=29 signal is a result of characteristic CO_2 fragmentation due to electron ionization in the mass spectrometer.

When CO_2 is pulsed over the catalysts which are in 5% H_2/Ar flow in dark at 400°C, the CO signal rises from the baseline values and water and methane appear as hydrogenation products. Catalyst illumination causes a change in product distribution by decreasing the methane and water formation, thus shifting the selectivity from Sabatier to RWGS reaction.

Supplementary note on Ni K-edge XAS analysis

Experimental details

Ni K-edge XANES and EXAFS spectra were measured in fluorescence detection mode at the BM23 beamline of the ESRF synchrotron radiation facility in Grenoble, France.

A Si(111) double crystal monochromator was used with energy resolution of about 1 eV at 8 keV. Higher-order harmonics were effectively eliminated by the flat mirror installed in front of the monochromator. The beam size on the sample was 4 mm horizontal and 0.2 mm vertical. The intensity of the monochromatic X-ray beam was measured by three consecutive ionization detectors, filled with appropriate nitrogen or argon gas mixtures to obtain 15% absorption in the first cell and 70% in the second and third cell. The first detector was filled with 300 mb Ar, second and third filled with 1400 mbar N_2. In all cases, the detectors were filled-up with He to the total pressure of 2 bars). The total X-ray absorption thickness (μd) of about 2.5 was obtained above the investigated Ni K-edge. A solid state SDD detector was used for X-ray fluorescence measurements. The Ni K-edge XANES and EXAFS spectra were measured in the energy region from -150 eV to +1000 eV relative to the investigated Ni K-edge. In XANES energy region, 0.3 eV steps were used and equidistant k steps of 0.03 $Å^{-1}$ in EXAFS region, with an integration time of 5 s/step. XAS spectra were measured in initial state on as-prepared catalyst in He at RT, and at stationary state during catalyst activation. Two or more repetitions of each scan were measured and superimposed to improve the signal-to-noise ratio. Exact energy calibration was provided by simultaneous measurements of absorption spectra on Ni metal foil placed between second and third ionization detectors. The first inflection point in the Ni metal K-edge is set at 8333 eV.

The analysis of the XANES and EXAFS spectra was performed with the Demeter (IFFEFIT) program package[10] in combination with the FEFF6 program code[11] for *ab initio* calculation of photoelectron scattering paths.

XANES supporting note

Different local environments of Ni cations lead to different K-edge profiles in the XANES region, and the energy position of the Ni K-edges correlate with the valence state of the metal cations in the sample.[12–15] The Ni K-edge profiles of the three catalysts in the initial state at RT are very similar, but not identical.

In-situ Ni K-edge XANES analysis is used to determine valence states of Ni cations in the as-synthesized catalysts and after activation in 10% H_2/He stream at 500°C, with and without visible light illumination. Normalized Ni K-edge XANES spectra are presented in Figure S15, together with the spectra of corresponding Ni reference compounds with different Ni valence states and local coordinations are shown for comparison.

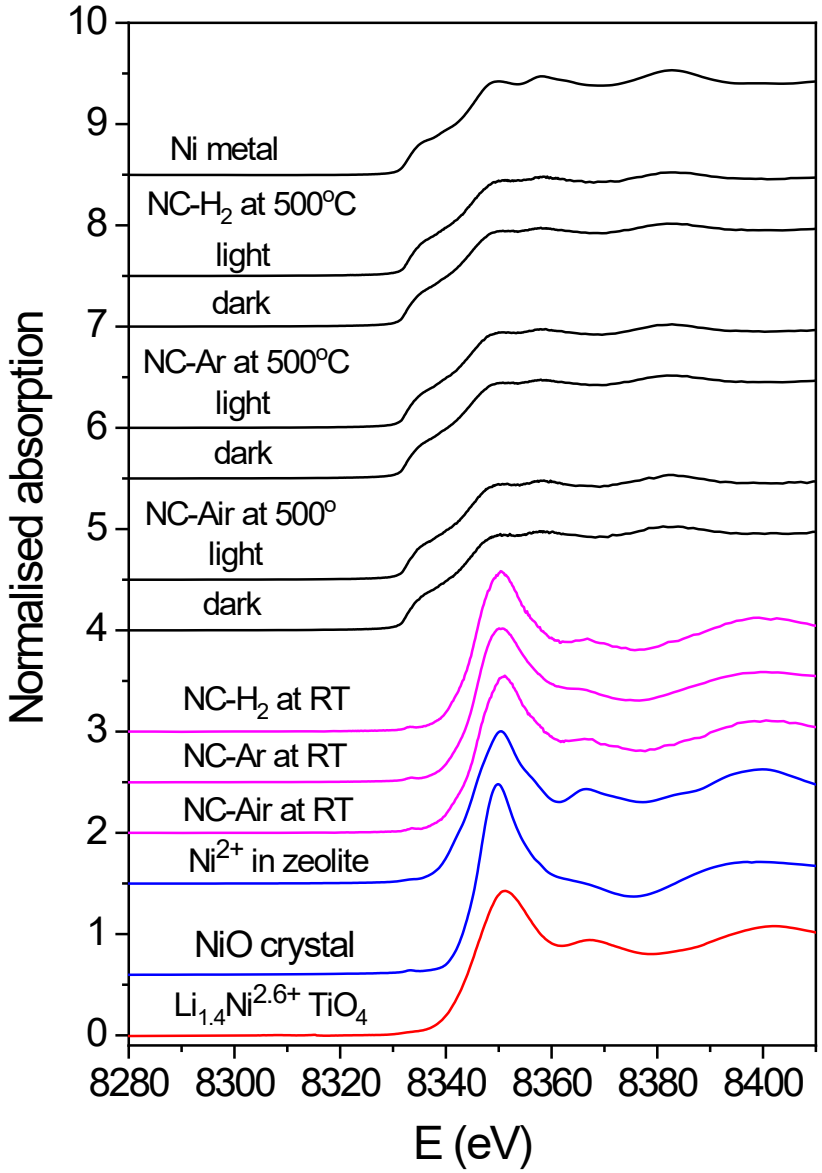

Figure S8. Normalized Ni K-edge XANES spectra of the NC-Air, NC-Ar and NC-H_2 as-synthesized catalysts and after activation in 10% H_2/He stream (flowrate of 27 ml/min) at 1 bar at 500°C, with and without visible light illumination (200 mW/cm^2). The spectra of reference Ni compounds with different Ni valence states and local coordination are shown for comparison (metallic Ni with fcc crystal structure, crystalline NiO with octahedrally coordinated Ni^{2+} cations, the Ni/ZSM-5 zeolite with Ni^{2+} cations with octahedral oxygen coordination, attached to the zeolite framework[16], and the crystalline $Li_{1.4}NiTiO_4$ cathode material for Li-Ion battery with 40% Ni^{2+} and 60% Ni^{3+} cations with octahedral oxygen coordination.[17,18]

We used a linear combination fit (LCF)[4],[10] of XANES spectra of reference Ni compounds with known valence states, the same or similar cation symmetry, the same type of neighboring atoms in the nearest coordination shells, arranged in a similar local structure, to

fully describe each XANES spectrum of the samples. In this way, the relative amounts of each type of Ni cation in different chemical and valence state in the sample was determined.

The (LCF) analysis shows that a linear combination of the following three XANES profiles can completely describe the XANES spectra of all the samples in initial state at RT: crystalline NiO with octahedrally coordinated Ni^{2+} cations, the Ni/ZSM-5 zeolite with Ni^{2+} cations with octahedral oxygen coordination, attached to the zeolite framework,[16] and the crystalline $Li_{1.4}NiTiO_4$ cathode material for Li-Ion battery with 40% Ni^{2+} and 60% Ni^{3+} cations with octahedral oxygen coordination.[17],[18] The goodness of the LCF fit is illustrated in Figure S16 for the XANES spectrum of the 2Ni-R H_2 sample. The relative amounts of Ni(0), Ni^{2+} and Ni^{3+} cations in the samples, deduced form the LCF analysis are listed in Table S2.

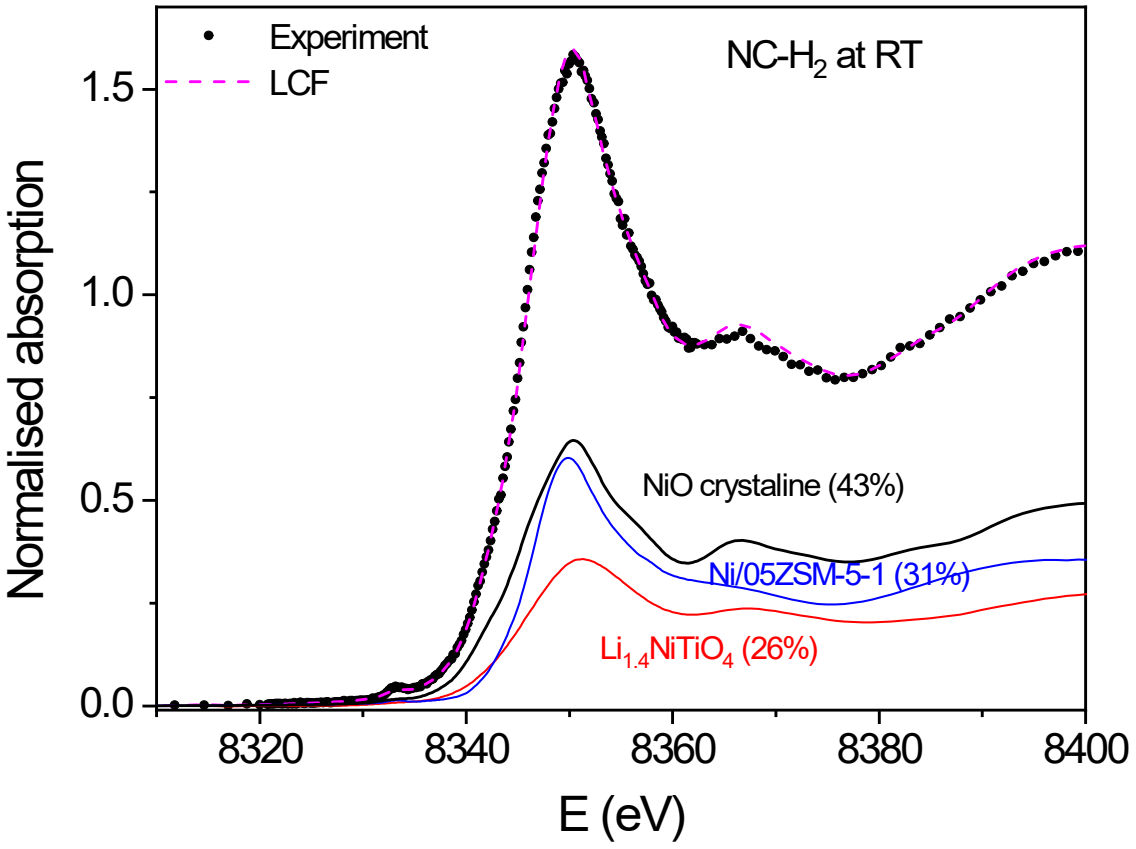

Figure S9. Ni K-edge XANES spectrum of the as-synthesized 2Ni-R H_2 sample: black squares: experiment; magenta dashed line: best fit with linear combination of the reference XANES profiles: NiO (43%) - black solid curve; Ni/ZSM-5 (31%) - blue solid curve, and $Li_{1.4}NiTiO_4$ (26%) - red solid curve.

Table S1. Relative amount of Ni^0, Ni^{2+} and Ni^{3+} cations in the samples, deduced form the LCF analysis. Uncertainties in the relative amounts are ± 2%.

Sample	**Ni^0 (%)**	**Ni^{2+} (%)**	**Ni^{3+} (%)**
NC-H_2 at RT	0	84	16
NC-Ar at RT	0	60	40
NC-Air at RT	0	52	48
NC-H_2 at 500°C/dark	100	0	0
NC-H_2 at 500°C/light	100	0	0
NC-Ar at 500°C/dark	100	0	0
NC-Ar at 500°C/light	100	0	0
NC-Air at 500°C/dark	100	0	0
NC-Air at 500°C/light	100	0	0

Ni K-edge EXAFS analysis

In-situ Ni K-edge EXAFS analysis is used to determine the local structure around Ni cations in the as-synthesized catalysts (NC-Air, NC-Ar and NC-H_2) and after activation in 10% H_2/He flow at 500°C, with and without visible light illumination. The analysis of the EXAFS spectra was performed with the Demeter (IFFEFIT) program package[10] in combination with the FEFF6 program code[11] for ab initio calculation of photoelectron scattering paths. Structural parameters of the average local Ni neighborhood (type and average number of neighbors, the radii and Debye-Waller factor of neighbor shells) are quantitatively resolved from the EXAFS spectra by comparing the measured EXAFS signal with model signal, constructed *ab initio* with the FEFF6 program code[11]. Two FEFF models are constructed, composed of neighbor atoms at distances characteristic for the expected Ni oxide and Ni metal species, indicated by XANES analysis of the catalyst at different states (at RT in air and after activation). The atomic species of neighbors are identified in the fit by their specific scattering factor and phase shift.

The FEFF model for Ni oxide is based on monoclinic crystal structure of NiO with space group *Fm3m* with the lattice constant a = 4.177 Å, where Ni is coordinated to 6 oxygen atoms at a distance of 2.08 Å, 12 Ni atoms at 2.95 Å and 8 oxygen atoms at 3.62 Å.[4] The FEFF model comprised three single scattering and two significant multiple scattering paths up to 4 Å, with 8 variable parameters: coordination shell distance (Δr) and Debye-Waller factors (σ^2) of all single scattering paths are introduced, and the amplitude reduction factor S_0^2, shift of energy origin of the photoelectron ΔE_o, common to all scattering paths. The shell coordination numbers were fixed to the crystallographic values. The structural parameters of multiple scattering paths are constrained to those of the corresponding single scattering paths. The model is tested on the EXAFS spectrum measured on crystalline NiO. A very

good EXAFS fit (Figure S17a) was obtained in the in the *k* range of 3 – 14 $Å^{-1}$ and the *R*-range of 1.2 – 3.3 Å. The best fit structural parameters are lined in the Table S3.

The Ni K-edge EXAFS spectra of the as-synthesized catalysts can be described by the FEFF model for crystalline NiO, where also the coordination shell numbers were allowed to vary. However, an additional coordination shell composed of Ce atoms at about 3.6 Å was introduced in the EXAFS model, to identify if there are the cations that are directly attached to the surface of the CeO_2 via Ni–O–Ce bridges. Very good fits (Figure S17a) are obtained in the in the *k* range of 3 – 12 $Å^{-1}$ and the *R*-range of 1.2 – 3.8 Å. The best fit structural parameters are listed in the Table S4.

Ni K-edge EXAFS spectra of the catalysts measured after activation in 10 % H_2/He flow at 500°C, with and without visible light illumination of the catalyst, were modelled with the Ni metal FEFF model, where also the coordination shell numbers were allowed to vary.

The FEFF model of fcc crystal structure of Ni metal with the lattice constant, a = 3.520 Å was composed of all four single and all multiple scattering paths up to 4.8 Å.[4] The model was calibrated by the Ni metal foil spectrum in the k range of 2 – 15 $Å^{-1}$ with six variable parameters: the amplitude reduction factor (S02), the shift of energy origin of the photoelectron (ΔEo), the lattice expansion (∆R/R), Debye temperature in modelling the Debye-Waller factors (σ2) of all paths except the first, for which a separate distance correction ∆r1 and Debye-Waller factor (σ2) were introduced. The shell coordination numbers were fixed at their *fcc* values (12, 6, 24, 12). The model precisely describes EXAFS spectrum measured on Ni metal foil (Figure S17b). The best fit structural parameters are lined in the Table S5. In addition, two scattering paths are added to the FEFF model (oxygen neighbors at 2.06 Å and Ce neighbors at 3.6 Å), as in case of the model for the as-synthesized catalysts to describe the EXAFS signal of eventual presence of Ni-O-Ce bridges. Three variable parameters for O and Ce shell of neighbors are introduced in the model: the shell coordination number (N), the distance (R) and the Debye-Waller factor (σ^2). The coordination numbers for O and Ce neighbors were constrained to the same value. A common shift of energy origin ΔE_o is allowed to vary. The amplitude-reduction factor S_0^2 is kept fixed at the value of 0.9. A good agreement between the model and the experimental spectra is found using the k range of 3 $Å^{-1}$ to 12 $Å^{-1}$ and the R range of 1.0 Å to 4.6 Å. Best fit results are presented in Figure S17b). The list of best fit parameters is given in Table S6.

The distribution of Ni neighbors is similar, but not identical to that in the Ni metal with *fcc* crystal structure. A splitting of the coordination shell at 4.31 Å is identified. The coordination numbers of Ni neighbors in all coordination shells is significantly lower than in the case of bulk metal with *fcc* structure, indicating that the average size of Ni metal clusters is below 1 nm in all samples. A presence of a small amount of O and Ce neighbors, at distances characteristic for Ni-O-Ce bridges (Table S4) is identified, which indicates attachment of Ni

clusters to CeO_2 support via Ni-O-Ce bridges.

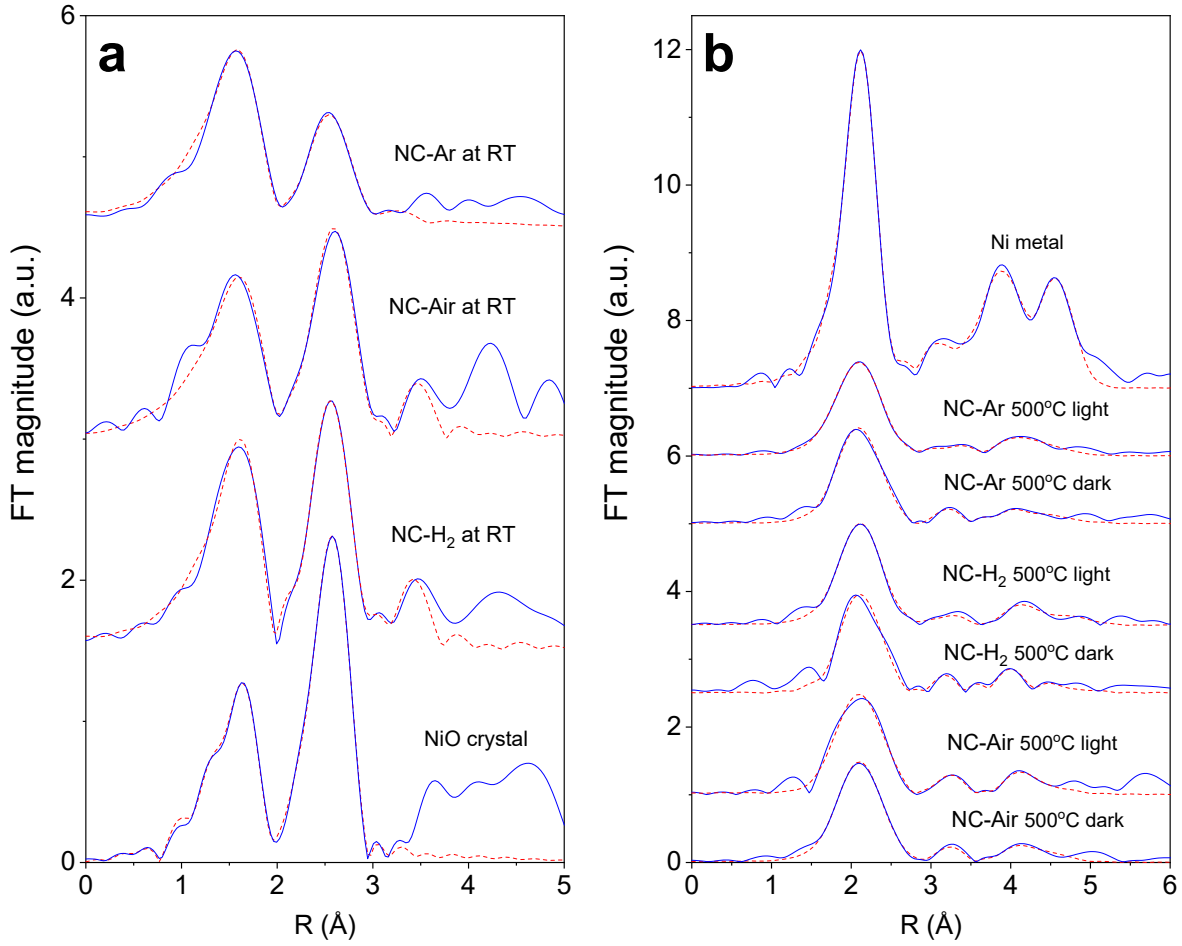

Figure S10. Fourier transform magnitude of k^2-weighted Ni K-edge EXAFS spectra in the k range of 3 –12 $Å^{-1}$ of the (a) as-synthesized NC-Air, NC-Ar and NC-H_2 catalysts and (b) in 10% H_2/He stream at 500°C, with and without visible light illumination. Experiment – (solid line); best fit EXAFS model calculated in the R range of 1 to 3.8 Å - (dashed line). The crystalline NiO and metal Ni reference spectrum are added for comparison. Spectra are shifted vertically for clarity.

Table S2. Parameters of the nearest coordination shells around Ni cations in the **crystalline NiO reference sample:** average number of neighbor atoms (N), distance (R), and Debye-Waller factor (σ^2). Uncertainty of the last digit is given in parentheses. A best fit is obtained with the amplitude reduction factor S_0^2=0.90(5) and the shift of the energy origin ΔE_o = -2(1) eV. The R-factor (quality of fit parameter) is listed in the last column.

Ni neigh.	*N*	*R* [Å]	σ^2 [$Å^2$]	*R*-factor
NiO crystaline				
O	6	2.080(5)	0.0047(5)	0.0016
Ni	12	2.952(2)	0.0053(5)	
O	8	3.42(3)	0.009(2)	

Table S3. Parameters of the nearest coordination shells around Ni cations in the **as-synthesized NC-Air, NC-Ar and NC-H_2 catalysts**: average number of neighbor atoms, distance (R), and Debye-Waller factor (σ^2). Uncertainty of the last digit is given in parentheses. A best fit is obtained with the amplitude reduction factor S_0^2=0.90(5) and the shift of the energy origin ΔE_o = -2(1) eV. The R-factor (quality of fit parameter), is listed in the last column.

Ni neigh.	N	R [Å]	σ2 [Å^2]	R-factor
NC-Ar				
O	6(1)	2.05(1)	0.009(1)	0.002
Ni	10(3)	2.99(1)	0.016(1)	
O	8(2)	3.22(3)	0.017(2)	
Ce	0.5(3)	3.54(2)	0.008(3)	

Ni neigh.	N*Ni rel	R [Å]	σ2 [Å^2]	R-factor
NC-Air				
O	6(1)	2.07(1)	0.010(1)	0.004
Ni	8(1)	2.99(1)	0.010(3)	
O	3(1)	3.64(3)	0.009(3)	
Ce	2(1)	3.64(2)	0.006(3)	

Ni neigh.	N*Ni rel	R [Å]	σ2 [Å^2]	R-factor
NC-H_2				
O	6(1)	2.06(1)	0.005(1)	0.006
Ni	7(2)	2.96(1)	0.007(1)	
O	4(1)	3.55(2)	0.009(2)	
Ce	2(1)	3.61(2)	0.005(3)	

Table S4. Parameters of the nearest coordination shells around Ni cations in the crystalline **Ni metal reference sample**: average number of neighbor atoms (N), distance (R), and Debye-Waller factor (σ^2). Uncertainty of the last digit is given in parentheses. A best fit is obtained with the amplitude reduction factor S_0^2=0.90(5) and the shift of the energy origin ΔE_o = -6 eV. The R-factor (quality of fit parameter) is listed in the last column.

Ni neigh.	*N*	*R* [Å]	σ^2 [Å^2]	*R*-factor
Ni metal (fcc)				
Ni	12	2.483(2)	0.0067(3)	0.0083
Ni	6	3.521(2)	0.009(1)	
Ni	24	4.313(3)	0.009(1)	
Ni	12	4.980(3)	0.009(1)	

Table S5. Parameters of the nearest coordination shells around Ni cations in the **NC-Air, NC-Ar and NC-H_2 catalysts after activation in 10% H_2/He stream at 500°C, with and without visible light illumination:** average number of neighbor atoms, distance (*R*), and Debye-Waller factor (σ^2). A combination of two FEFF models is used: Ni metal with fcc crystal structure and Ni-O-Ce model to describe Ni cations directly attached to the CeO_2 support. Uncertainty of the last digit is given in parentheses. A best fit is obtained with the amplitude reduction factor S_0^2=0.90(5) and the shift of the energy origin ΔE_o = 3(2) eV. *R*-factor (quality of fit parameter) is listed in the last column.

Ni neigh.	*N*	*R* [Å]	σ^2 [Å^2]	*R*-factor
NC-H_2 dark				
Metallic Ni				
Ni	9(1)	2.45(1)	0.016(1)	0.037
Ni	2(1)	3.35(7)	0.016(1)	
Ni	8(1)	4.00(4)	0.013(2)	
Ni	12(1)	4.23(4)	0.013(2)	
Ni	2(1)	4.94(4)	0.016(2)	
Ni-O-Ce bridges				
O	0.6(2)	2.08(1)	0.003(1)	
Ce	0.6(2)	3.54(9)	0.003(1)	

Ni neigh.	*N*	*R* [Å]	σ^2 [Å^2]	*R*-factor
NC-H_2 light				
Metallic Ni				
Ni	8(1)	2.45(1)	0.015(2)	0.012
Ni	2(1)	3.41(4)	0.015(2)	
Ni	6(1)	4.08(4)	0.015(2)	
Ni	8(1)	4.31(4)	0.015(2)	
Ni	1(1)	5.06(4)	0.015(2)	
Ni-O-Ce bridges				
O	0.3(2)	2.06(1)	0.003(1)	
Ce	0.3(2)	3.53(4)	0.003(2)	

Ni neigh.	*N*	*R* [Å]	σ^2 [Å^2]	*R*-factor
NC-Air dark				
Metallic Ni				
Ni	10(1)	2.46(1)	0.017(1)	0.004
Ni	2(1)	3.44(4)	0.017(1)	
Ni	4(2)	4.05(4)	0.017(2)	
Ni	6(2)	4.28(4)	0.017(2)	
Ni	8(3)	4.78(4)	0.017(2)	
Ni-O-Ce bridges				
O	0.3(2)	2.03(1)	0.003(1)	
Ce	0.3(2)	3.53(9)	0.003(1)	

Ni neigh.	*N*	*R* [Å]	σ^2 [Å^2]	*R*-factor
NC-Air light				
Metallic Ni				
Ni	12(1)	2.46(1)	0.019(2)	0.017
Ni	3(1)	3.39(4)	0.019(2)	
Ni	7(3)	4.06(4)	0.019(2)	
Ni	12(3)	4.30(4)	0.019(2)	
Ni	11(3)	4.76(4)	0.019(2)	
Ni-O-Ce bridges				
O	0.6(2)	2.01(1)	0.003(1)	
Ce	0.6(2)	3.53(8)	0.003(2)	

Ni neigh.	*N*	*R* [Å]	σ^2 [Å^2]	*R*-factor
NC-Ar dark				
Metallic Ni				
Ni	9(1)	2.45(1)	0.017(1)	0.009
Ni	2(1)	3.39(7)	0.017(1)	
Ni	5(2)	4.03(4)	0.017(2)	
Ni	7(2)	4.25(4)	0.017(2)	
Ni	7(3)	4.80(4)	0.017(2)	
Ni-O-Ce bridges				
O	0.5(2)	2.04(1)	0.003(1)	
Ce	0.5(2)	3.50(9)	0.003(1)	

Ni neigh.	*N*	*R* [Å]	σ^2 [Å^2]	*R*-factor
NC-Ar light				
Metallic Ni				
Ni	10(1)	2.45(1)	0.017(2)	0.003
Ni	2(1)	3.39(4)	0.017(2)	
Ni	5(3)	4.02(4)	0.017(2)	
Ni	8(3)	4.27(4)	0.017(2)	
Ni	10(3)	4.79(4)	0.017(2)	
Ni-O-Ce bridges				
O	0.3(2)	2.00(1)	0.003(1)	
Ce	0.3(2)	3.59(8)	0.003(2)	

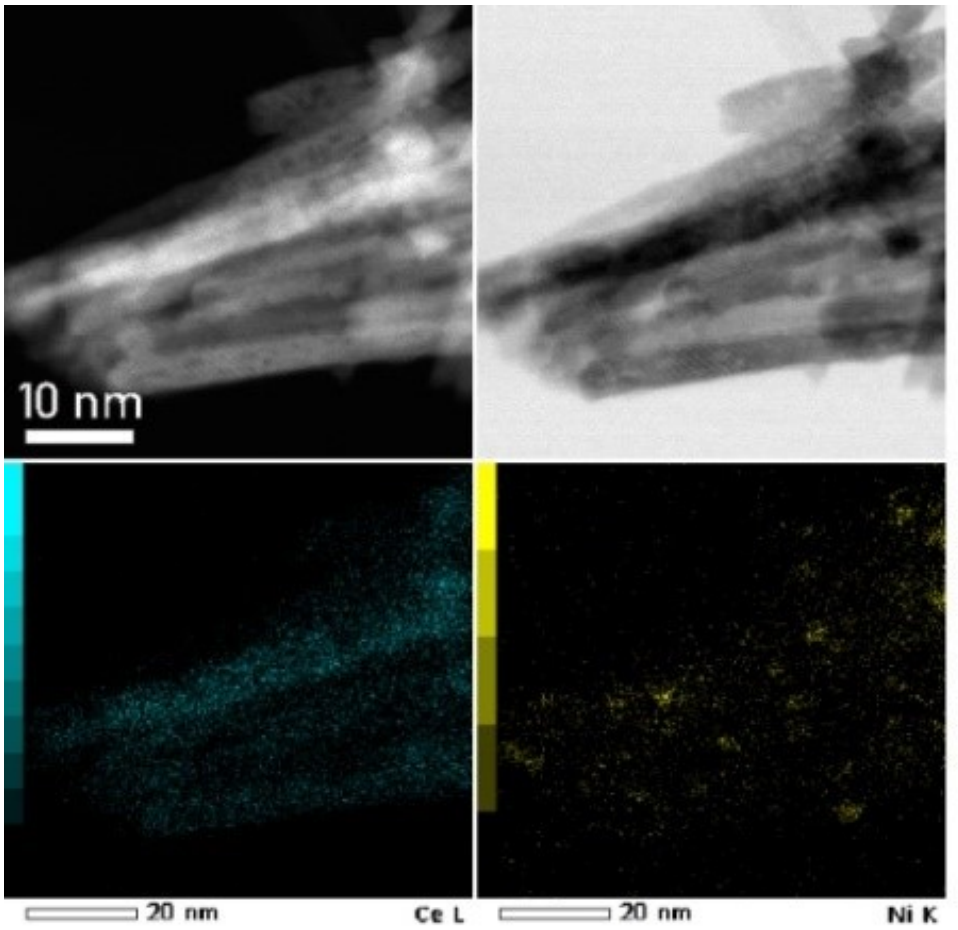
10 nm
20 nm
Ce L
20 nm
Ni K

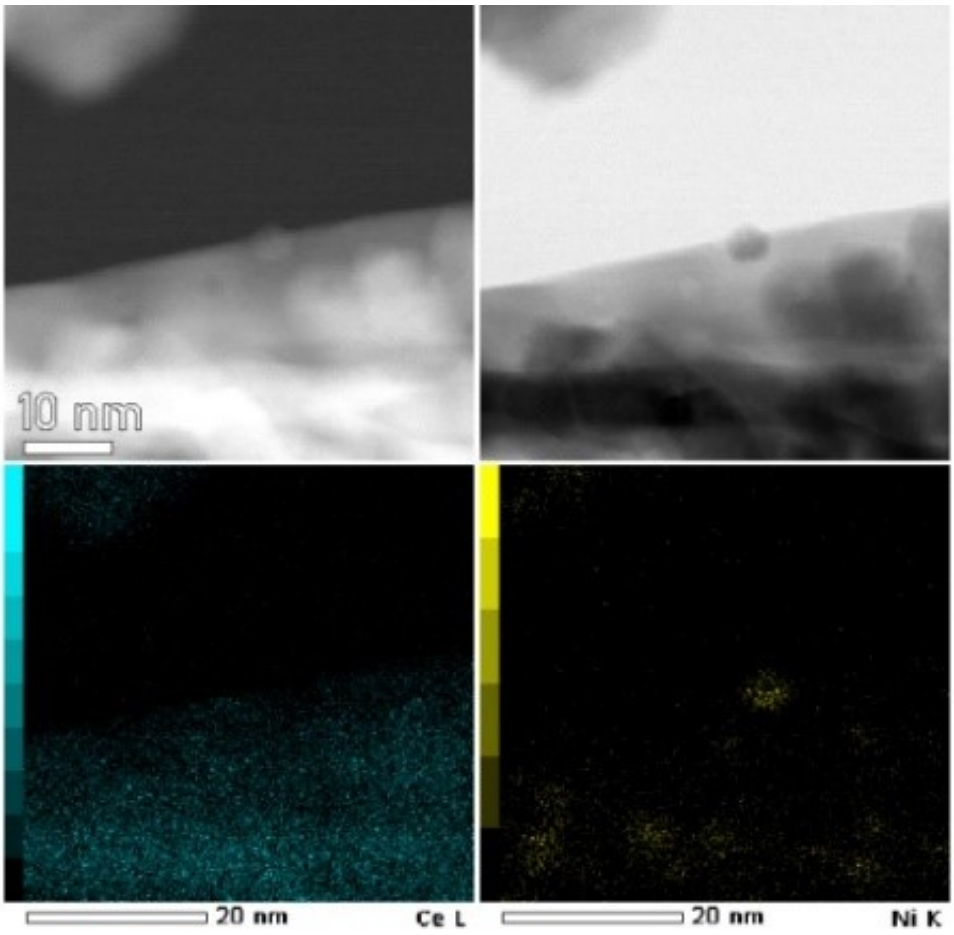
10 nm
20 nm
Ce L
20 nm
Ni K

Figure S11. HAADF- and BF-STEM micrographs of NC-H_2 catalyst and corresponding Ce-L and Ni-K EDS maps.

Supplementary note on Raman analysis

For bare ceria supports, initial Raman spectra recorded at RT in air are very similar (Figure S8). It has to be noted that ceria reduction is initiated on its surface with cleavage of C-H bond of methane, followed by hydrogen atoms reacting with surface oxygen, water formation and desorption.

Stepwise heating of samples in CH_4/CO_2 flow continuously increases the signal between 500-600 cm^{-1}, indicating progressively more abundant oxygen defects are present in the subsurface. This due to lattice oxygen diffusion to the surface as a result of concentration gradients. It is also known that most stable, partly reduced form of ceria (111) facet prefers subsurface oxygen migration to the surface and accumulation of oxygen vacancies in the bulk[4],[5].

The vibration mode of surface oxygen (band at 240cm^{-1}) goes through a maximum between 300-400°C and decays somewhat at 500°C (Figure S8), stabilizing at values that are comparable to the ones at 25°C in air (Table 1 in manuscript). Transient surface enrichment with oxygen is likely related to faster diffusion of subsurface oxygen to surface, compared to methane dissociation on bare ceria. As a result of this transient process, surface and bulk oxygen modes show different trends: no net-loss of surface oxygen occurs during exposure to CH_4/CO_2 flow, whereas subsurface reduction is meaningful.

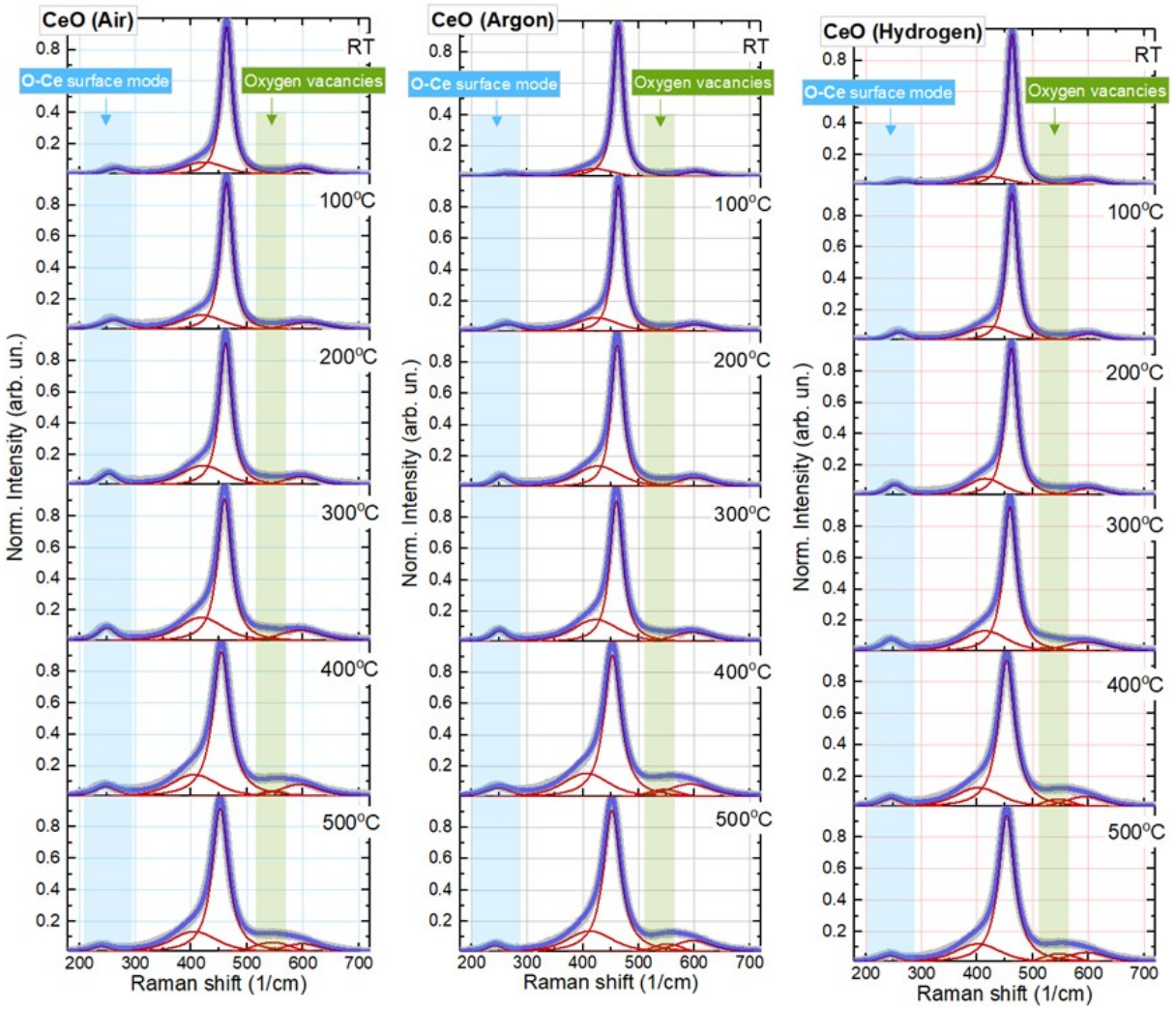

Figure S12. Temperature-dependent Raman spectra for bare CeO_2 calcined in air, argon or hydrogen when exposed to equimolar CH_4/CO_2 flow.

Once Ni clusters are distributed over the CeO_2, the area under the “surface mode” peak corresponding to the O-Ce (111) longitudinal stretching motions within the outer layers is reduced (Figure S9). This is likely caused by nickel covering about 0.05 ML of the ceria surface (assuming 50% nickel dispersion) and abundant oxygen defects present already at room temperature. At 500°C, the surface oxygen vibrational mode is negligible (Table 1), which is due to much faster methane dissociation on nickel and fast reaction between spilled over hydrogen and surface oxygen atoms from ceria. Ni clusters increase the contribution of anion vacancies or, they activate the movement of oxygen from the inner crystalline sites to the outer sites on the surface and stimulate the release of oxygen from these sites.[6] Also, bulk oxygen defect signals increase progressively with temperature and reaches 1.1, 1.9 and 2.1 times higher values compared to bare ceria as a result of calcination in air, argon or hydrogen. To summarize: nickel has a profound effect on both surface and bulk oxygen defect density.

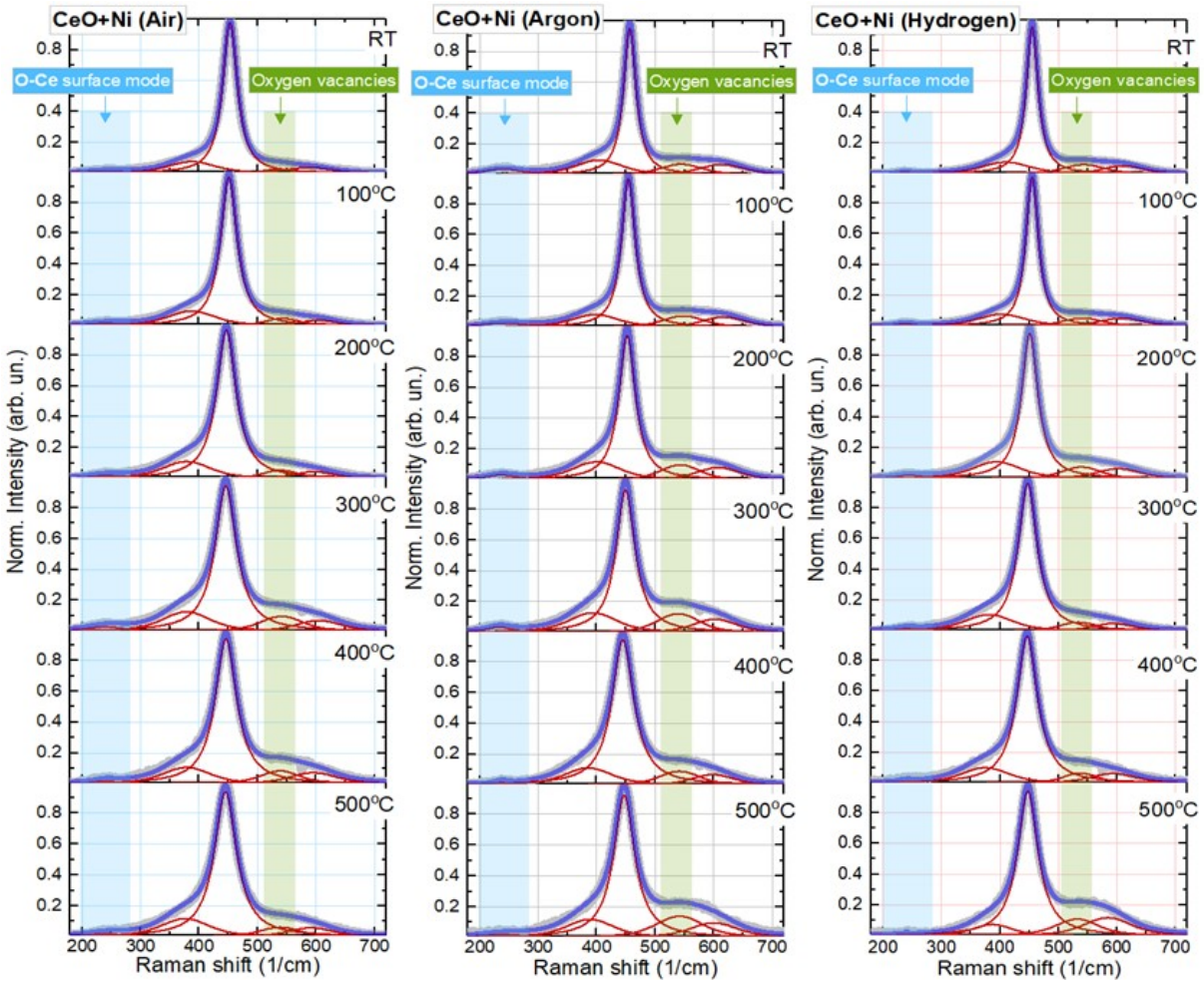

Figure S13. Temperature-dependent Raman spectra for $2Ni/CeO_2$ catalysts calcined in air, argon or hydrogen when exposed to equimolar CH_4/CO_2 flow.

Table S6. Specific surface area, total pore volume, average pore size diameter, unit cell size and volume and the average crystallite size for different CeO_2 morphologies before and after deposition of 2 wt. % nickel. Size of Ni was determined by analysis of *in-situ* XAS data.

Sample	S_{BET} (m^2/g)	V_{pore} (cm^3/g)	a (Å)	V ($Å^3$)	CeO_2 crystal size (nm)	XANES/EXAFS Ni size (nm)
CeO_2-Air	85	0.30	5.4138(5)	158.67	12.2	/
CeO_2-Ar	85	0.25	5.4145(3)	158.74	12.9	/
CeO_2-H_2	87	0.26	5.4155(2)	158.83	12.1	/
NC-Air	82	0.32	5.410(1)	158.38	12.5	< 1
NC-Ar	84	0.26	5.410(1)	158.38	11.3	< 1
NC-H_2	85	0.28	5.411(2)	158.47	11.4	< 1

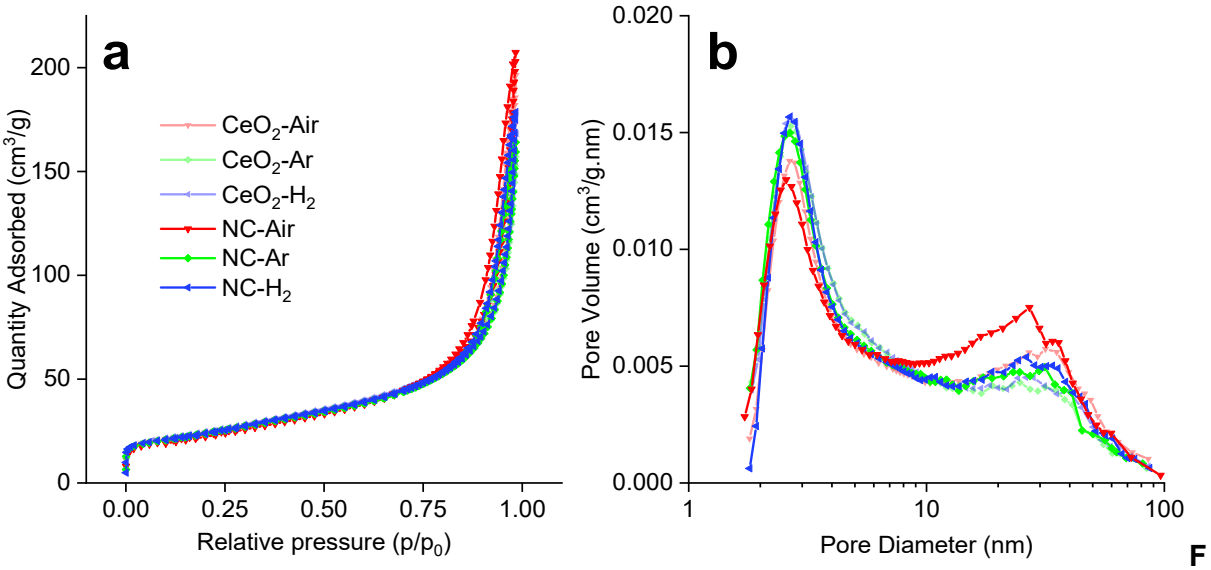

igure S14. (a) N_2 physisorption isotherms and (b) pore size distribution for CeO_2 supports before and after deposition of 2 wt. % nickel calcined in Air, Ar and H_2 atmospheres.

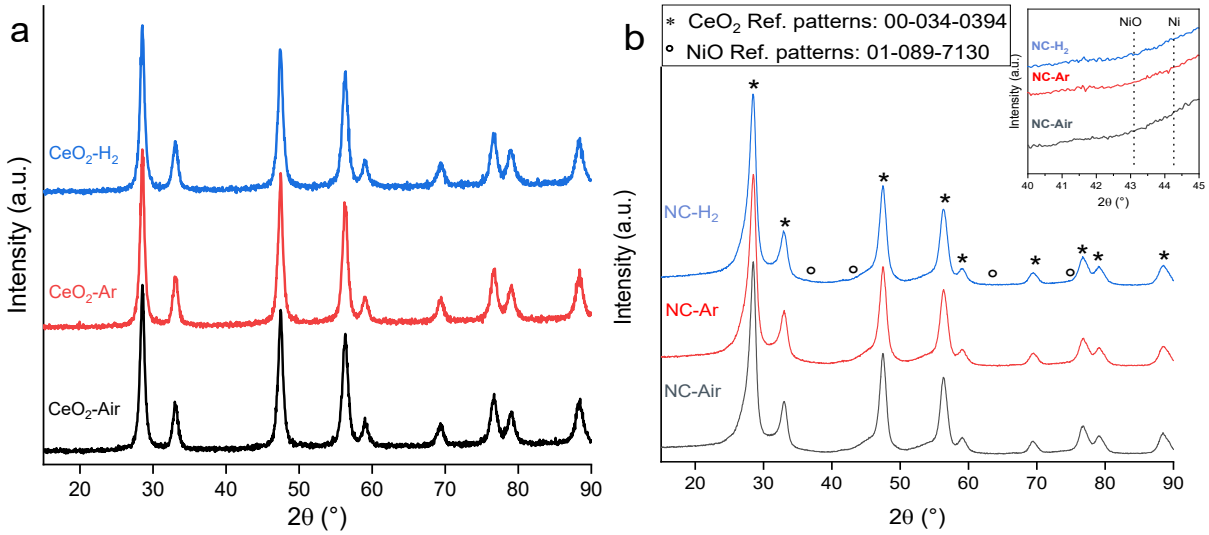

Figure S15. XRD patterns of a) bare CeO_2 nanorod supports and b) 2Ni/CeO_2 catalysts calcined in H_2, Ar and Air atmosphere. Inset shows magnified 2 theta region where the most intense diffraction lines from NiO [200] and Ni [111] (cubic, *Fm-3m* phase) are expected.

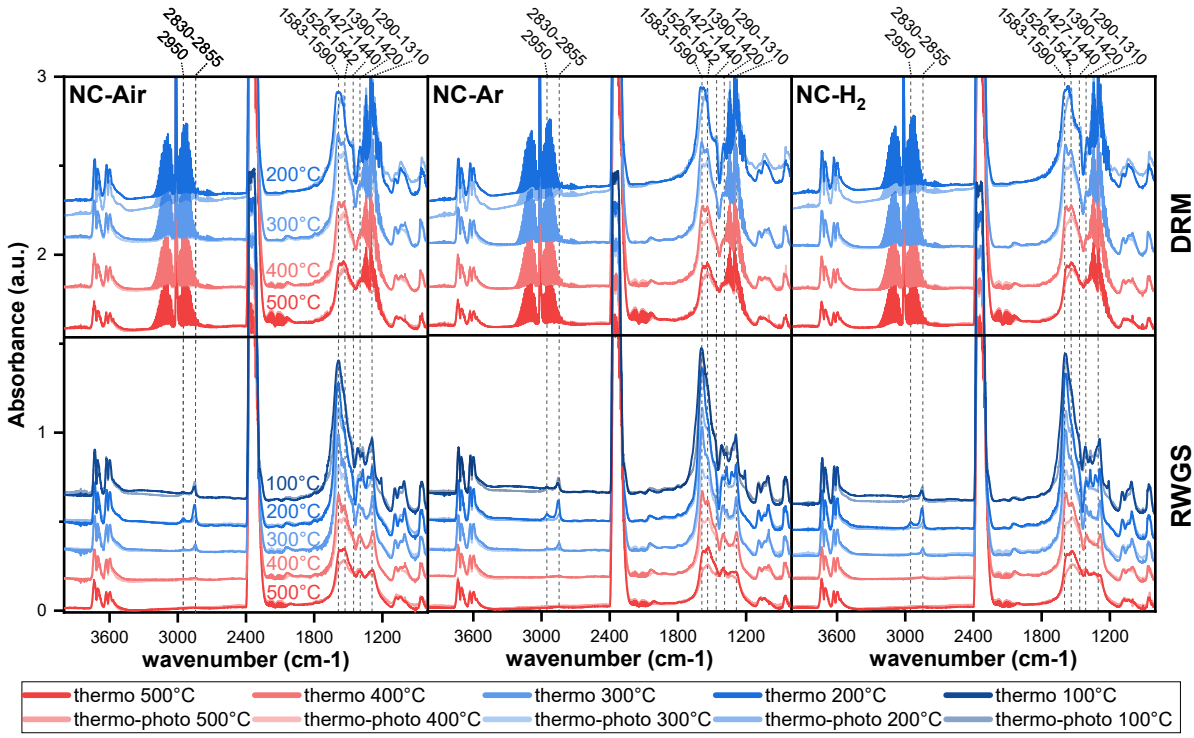

Figure S16. Full operando DRIFT spectra of DRM and RWGS analyses at different temperatures in thermo and photo-thermal modes for NC-Air, NC-Ar and NC-H_2 catalysts.

Assignation of carbonate vibrations during operando DRIFT DRM and RWGS analysis

Due to the complexity and overlapping contributions of individual vibrations in the obtained CO_2-DRIFTS spectra, reliable peak assignment and identification of carbonate species is not trivial. In order to be able to assign the COO vibrations to the carboxylate groups, both asymmetric ($\nu_{as}COO^-$; 1650 - 1520 cm^{-1}) and symmetric (ν_sCOO^-; 1450 - 1360 cm^{-1}) vibrations must be present simultaneously. Bands characteristic of different carbonates on ceria were observed in the range between 1200 and 1700 cm^{-1}: Monodentate (M), bidentate (B), polydentate (P) and hydrogen carbonate (HC).[7] The existence of peaks in the $\nu_{as}COO^-$ vibrational range can be categorized as bidentate carbonate (1520 - 1570 cm^{-1}), monodentate carbonate and hydrogen carbonate (M, HC 1580 – 1610 cm^{-1}).[7]-[8] The bands between 1490 and 1385 cm^{-1} are assigned to the presence of polydentate carbonates on ceria. The vibrations between 3000 cm^{-1} and 2700 cm^{-1} are characteristic of the stretching of the C-H bond.[9] Under DRM and RWGS reaction conditions, characteristic peaks appear between 1360 - 1450 cm^{-1}, 1520 – 1650 cm^{-1} and 2700 – 2950 cm^{-1}, indicating symmetric and asymmetric COO^- vibrations as well as C-H stretching and bending vibrations, thus revealing the population of catalytic surfaces with bidentate and monodentate formate species. As the temperature decreases, the population of carbonate increases. Once the

catalysts are illuminated with visible light, the opposite effect occurs, with the intensity of the bidentate and monodentate carbonates decreasing. It can be concluded that under photo-thermal DRM and RWGS reaction conditions, the bidentate and monodentate carbonates desorb, convert to CO or transform into stable polydentate carbonate (increase in bands between 1490 and 1385 cm^{-1}).

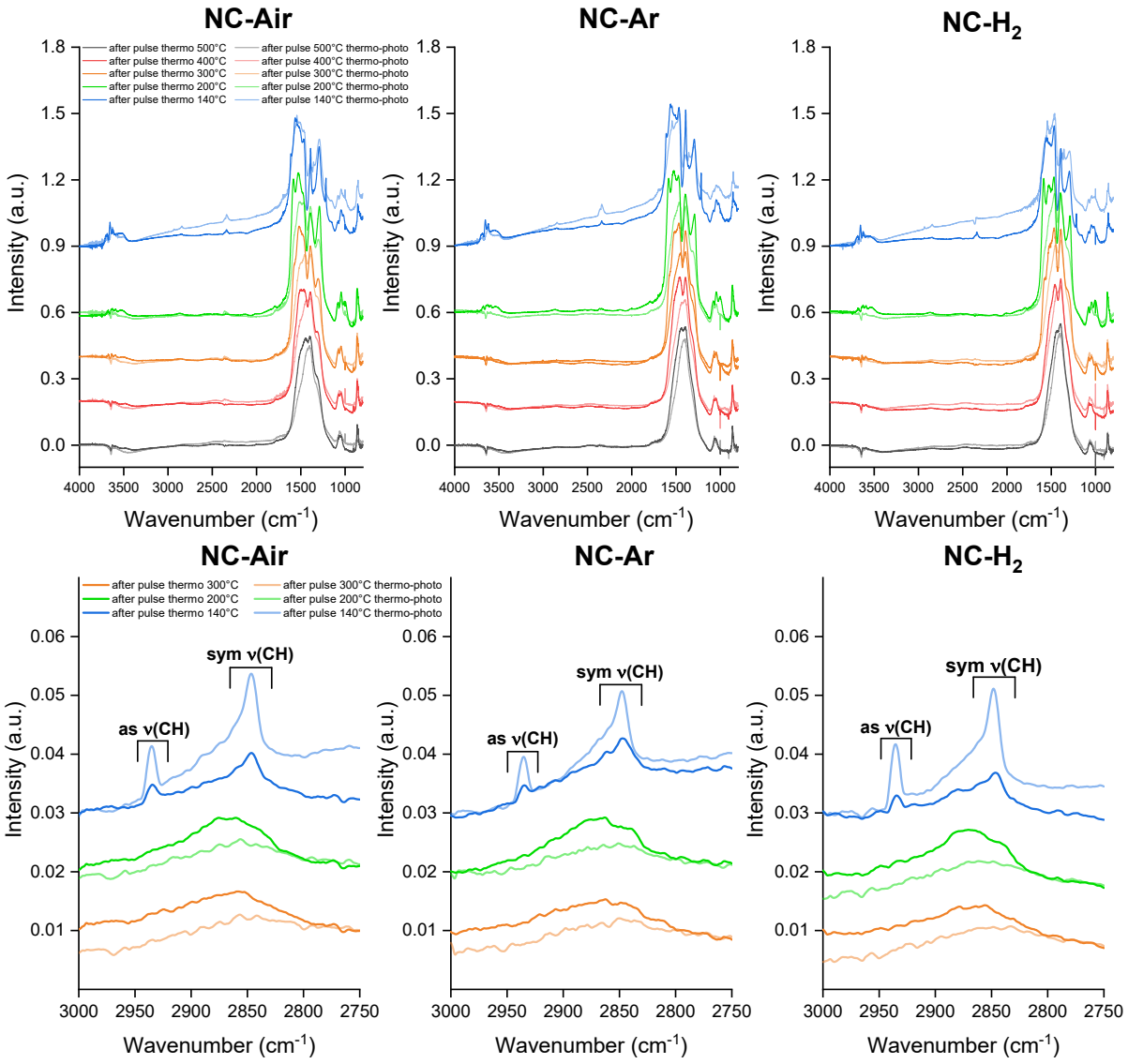

Figure S17. Full DRIFT spectra after pulses of DRM mixture (50:50, CH_4:CO_2) during thermal and photo-thermal conditions at different temperatures over NC-Air, NC-Ar and NC-H_2 catalysts (upper panel). DRIFT spectra of CH bond vibrations region after DRM mixture pulses, under thermal and photo-thermal condition between 300 °C and 140 °C temperature range for NC-Air, NC-Ar and NC-H_2 catalysts (lower panel).

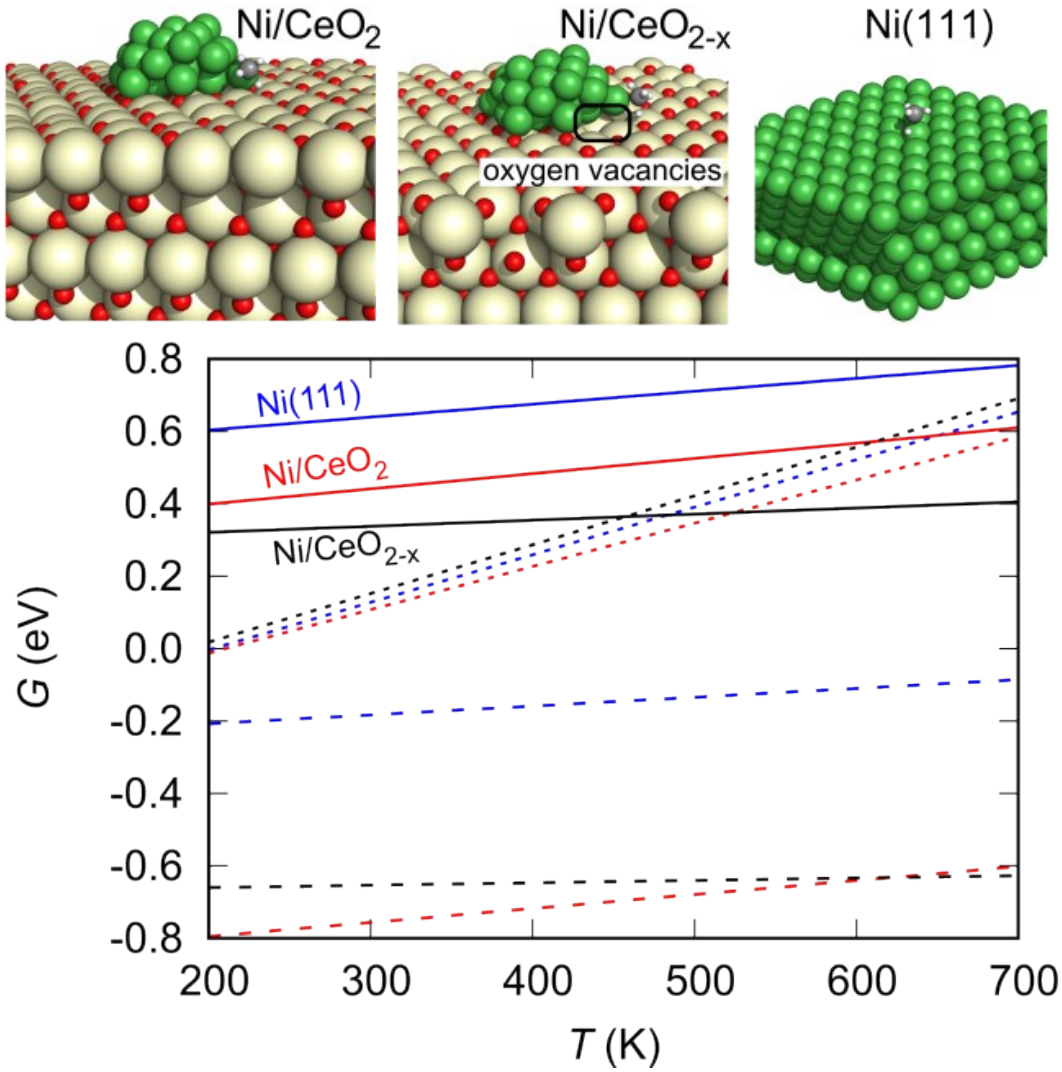

Figure S18. Top panel shows transition state structures for the reaction step: CH_4* + * → CH_3* + H* on $Ni_{34}/(CeO_2)_n$, $Ni_{34}/(CeO_{2-x})_n$, Ni(111). The bottom panel shows Gibbs free energy of CH_4 adsorption (dotted line), Gibbs free energy of CH_4 activation (solid line), and Gibbs free energy change during the reaction step (dashed line) on $Ni_{34}/(CeO_2)_n$ (red), $Ni_{34}/(CeO_{2-x})_n$ (black), Ni(111) (blue).

References

[1] O. Levenspiel, Chemical Reaction Engineering, third edit, Wiley and Sons, 1999.

[2] V. Subramanian, E.E. Wolf, P. V. Kamat, Catalysis with TiO_2/Gold Nanocomposites. Effect of Metal Particle Size on the Fermi Level Equilibration, J. Am. Chem. Soc. 126 (2004) 4943–4950. doi:10.1021/ja0315199.

[3] X. Li, J. Yu, M. Jaroniec, X. Chen, Cocatalysts for Selective Photoreduction of CO_2 into Solar Fuels, Chem. Rev. 119 (2019) 3962–4179. doi:10.1021/acs.chemrev.8b00400.

[4] K. Lorber, J. Zavašnik, I. Arčon, M. Huš, J. Teržan, B. Likozar, P. Djinović, CO_2 Activation over Nanoshaped CeO_2 Decorated with Nickel for Low-Temperature Methane Dry Reforming, ACS Appl. Mater. Interfaces. 14 (2022) 31862–31878. doi:10.1021/acsami.2c05221.

[5] G.E. Murgida, M.V. Ganduglia-Pirovano, Evidence for Subsurface Ordering of Oxygen Vacancies on the Reduced CeO_2 (111) Surface Using Density-Functional and Statistical Calculations, Phys. Rev. Lett. 110 (2013) 246101. doi:10.1103/PhysRevLett.110.246101.

[6] F. Zhang, Z. Liu, X. Chen, N. Rui, L.E. Betancourt, L. Lin, W. Xu, C.-J. Sun, A.M.M. Abeykoon, J.A. Rodriguez, J. Teržan, K. Lorber, P. Djinović, S.D. Senanayake, Effects of Zr Doping into Ceria for the Dry Reforming of Methane over Ni/$CeZrO_2$ Catalysts: *In Situ* Studies with XRD, XAFS, and AP-XPS, ACS Catal. 10 (2020) 3274–3284. doi:10.1021/acscatal.9b04451.

[7] G.N. Vayssilov, M. Mihaylov, P. St. Petkov, K.I. Hadjiivanov, K.M. Neyman, Reassignment of the Vibrational Spectra of Carbonates, Formates, and Related Surface Species on Ceria: A Combined Density Functional and Infrared Spectroscopy Investigation, J. Phys. Chem. C. 115 (2011) 23435–23454. doi:10.1021/jp208050a.

[8] S.-C. Yang, S.H. Pang, T.P. Sulmonetti, W.-N. Su, J.-F. Lee, B.-J. Hwang, C.W. Jones, Synergy between Ceria Oxygen Vacancies and Cu Nanoparticles Facilitates the Catalytic Conversion of CO_2 to CO under Mild Conditions, ACS Catal. 8 (2018) 12056–12066. doi:10.1021/acscatal.8b04219.

[9] Z. Wu, A.K.P. Mann, M. Li, S.H. Overbury, Spectroscopic Investigation of Surface-Dependent Acid–Base Property of Ceria Nanoshapes, J. Phys. Chem. C. 119 (2015) 7340–7350. doi:10.1021/acs.jpcc.5b00859.

[10] B. Ravel, M. Newville, ATHENA , ARTEMIS , HEPHAESTUS : data analysis for X-ray absorption spectroscopy using IFEFFIT, J. Synchrotron Radiat. 12 (2005) 537–541. doi:10.1107/S0909049505012719.

[11] J.J. Rehr, R.C. Albers, S.I. Zabinsky, High-order multiple-scattering calculations of x-ray-absorption fine structure, Phys. Rev. Lett. 69 (1992) 3397–3400. doi:10.1103/PhysRevLett.69.3397.

[12] M. Zabilskiy, I. Arčon, P. Djinović, E. Tchernychova, A. Pintar, In-situ XAS study of catalytic N_2O decomposition over CuO/CeO_2 catalysts, ChemCatChem. (2021) cctc.202001829. doi:10.1002/cctc.202001829.

[13] N.N. Tušar, D. Maučec, M. Rangus, I. Arčon, M. Mazaj, M. Cotman, A. Pintar, V. Kaučič, Manganese functionalized silicate nanoparticles as a Fenton-type catalyst for water purification by Advanced Oxidation Processes, Adv. Funct. Mater. 22 (2012) 820–826.

doi:10.1002/adfm.201102361.

[14] I. Arčon, J. Kolar, A. Kodre, D. Hanžel, M. Strlič, XANES analysis of Fe valence in iron gall inks, X-Ray Spectrom. 36 (2007) 199–205. doi:https://doi.org/10.1002/xrs.962.

[15] R. Dominko, C. Sirisopanaporn, C. Masquelier, D. Hanzel, I. Arcon, M. Gaberscek, On the Origin of the Electrochemical Capacity of $Li_2Fe_{0.8}Mn_{0.2}SiO_4$, J. Electrochem. Soc. 157 (2010) A1309. doi:10.1149/1.3491368.

[16] H.-T. Vu, I. Arčon, D.O. de Souza, S. Pollastri, G. Dražić, J. Volavšek, G. Mali, N. Zabukovec Logar, N. Novak Tušar, Insight into the interdependence of Ni and Al in bifunctional Ni/ZSM-5 catalysts at the nanoscale, Nanoscale Adv. 4 (2022) 2321–2331. doi:10.1039/D2NA00102K.

[17] M. Kuzma, I. Arčon, A. Dominko, Robert Gaberšček, Miran Kodre, J. Padežnik Gomilšek, *In situ* XANES and EXAFS Study of $Li_{2-x}NiTiO_4$ cathode material for Li-ion batteries, Hamburg, 2009. http://photon-science.desy.de/annual_report/files/2009/2009515.pdf.

[18] M. Küzma, R. Dominko, A. Meden, D. Makovec, M. Bele, J. Jamnik, M. Gaberšček, Electrochemical activity of Li_2FeTiO_4 and Li_2MnTiO_4 as potential active materials for Li ion batteries: A comparison with Li_2NiTiO_4, J. Power Sources. 189 (2009) 81–88. doi:10.1016/j.jpowsour.2008.11.015.